Characterization and dynamics of the auroral electron precipitation during substorms deduced from IMAGE-FUV

M. Meurant,[1] J. C. Gérard,[1] B. Hubert,[1] V. Coumans,[1] V. I. Shematovich,[2] D. V. Bisikalo,[2] D. S. Evans,[3] G. R. Gladstone,[4] and S. B. Mende[5]

Received 13 September 2002; revised 10 January 2003; accepted 27 February 2003; published 20 June 2003.

[1] The FUV imager on board the IMAGE satellite provides simultaneous images of the north polar aurora every 2 min in three spectral channels. The Wideband Imaging Camera (WIC) responds primarily to the N_2 LBH bands while one of the Spectral Imagers (SI13) includes the OI 135.6 nm emission and nearby LBH bands. The third channel (SI12) is sensitive to Doppler-shifted Lyman-α emission at 121.8 nm generated by proton precipitation. The relative magnitude of the WIC and SI13 signals depends on the altitude distribution of the energy deposition, in response to the differential O_2 absorption and the altitude dependence of the neutral composition. The ratio of simultaneous images from WIC and SI13 is used to derive the spatial distribution of the characteristic energy of the precipitating auroral electrons and the energy flux they carry. The method is described and the uncertainties introduced by possible perturbations of the neutral composition known to occur in the auroral thermosphere are discussed. The first part of this study describes a validation of this method performed by comparing precipitation characteristics derived from FUV with in situ measurements from two coincident passes of the NOAA-16 satellite. They are shown to agree within about 45%. The second part applies this ratio method to analyze the time evolution of auroral activity which occured during two substorms on 28 October 2000. The time evolution is displayed in the form of magnetic local time and magnetic latitude keograms. It is shown that the pattern of the electron average energy distribution exhibits both spatial and temporal changes. Comparison with FAST in situ electron spectrograms confirms the ability of IMAGE to detect precipitation events with a $\sim$200 km spatial scale. However the characteristics of the physical process leading to electron acceleration cannot be identified with FUV. The highest values of the average energy are colocated in time and space with the largest electron precipitation fluxes. A dawnward motion of bright features is observed in the postmidnight at speeds on the order of 5 magnetic local time hours/UT hour. *INDEX TERMS:* 2704 Magnetospheric Physics: Auroral phenomena (2407); 2716 Magnetospheric Physics: Energetic particles, precipitating; 2788 Magnetospheric Physics: Storms and substorms; 2794 Magnetospheric Physics: Instruments and techniques; *KEYWORDS:* auroral electron energy, global FUV imaging, auroral substorm, NOAA and FAST satellites

Citation: Meurant, M., J. C. Gérard, B. Hubert, V. Coumans, V. I. Shematovich, D. V. Bisikalo, D. S. Evans, G. R. Gladstone, and S. B. Mende, Characterization and dynamics of the auroral electron precipitation during substorms deduced from IMAGE-FUV, *J. Geophys. Res.*, *108*(A6), 1247, doi:10.1029/2002JA009685, 2003.

1. Introduction

[2] Far ultraviolet (FUV) imaging systems from space-based platforms have played a key role in visualizing global auroral activity and understanding its complex auroral morphology and dynamics [*Craven and Frank*, 1987]. Global FUV images have also been used to determine the energy flux precipitated over the entire auroral oval, a quantity known as the total hemispheric power [*Lummerzheim et al.*, 1997; *Hubert et al.*, 2002], total energy dissipation [*Østgaard et al.*, 2001], or global auroral power [*Meng and Liou*, 2002]. This quantity is an important indicator to quantify the global amount of ionization and heat produced in the thermosphere, but it does not provide any quantitative information on the characteristic energy of the incoming particles or their spatial distribution.

[3] The POLAR UltraViolet Imager (UVI) was used to estimate the incident energy characteristics from a comparison of consecutive images obtained in two spectral regions

[1]Laboratoire de Physique Atmosphérique et Planétaire, Institut d'Astrophysique et de Géophysique, Université de Liège, Liège, Belgium.
[2]Institute of Astronomy, Russian Academy of Sciences, Moscow, Russia.
[3]Space Environment Laboratory, National Oceanic and Atmospheric Administration, Boulder, Colorado, USA.
[4]Southwest Research Institute, San Antonio, Texas, USA.
[5]Space Sciences Laboratory, University of California, Berkeley, California, USA.

0148-0227/03/2002JA009685$09.00

with differential absorption by the overlying O_2 column [*Germany et al.*, 1997]. The mean energy determined in this way was compared with in situ measurements from an overflight of the DMSP-12 satellite. A satisfactory agreement was found with the remotely determined electron energy, except near the poleward oval and boundary where the brightness increased between the two UVI images. *Chua et al.* [2001] showed an example indicating that the electron mean energies derived from UVI are in good agreement with FAST but systematically overestimated. The images obtained with POLAR UVI in two wavelengths are not coincident in time, which restricts the application of this method to periods of moderate or low time variations.

[4] Previous direct comparisons with the IMAGE-FUV images have used in situ electron and proton measurements from the FAST, DMSP, and NOAA satellites [*Frey et al.*, 2001; *Gérard et al.*, 2001; *Coumans et al.*, 2002]. They have shown that the brightness of the auroral emissions excited at the footprint of the magnetic field line passing through the low-altitude satellite is generally in good agreement with the values expected from model calculations using in situ measurements of the particle energy spectra. Based on measurements of the incident electron and proton spectra carried over 10 auroral NOAA passes, *Coumans et al.* [2002] predicted FUV signals statistically within 25% of the observations for WIC and 40% for SI12. However, such direct validations do not necessarily imply that the emissions can be used quantitatively to inversely determine the characteristics of the precipitating electrons.

[5] In this study we first show that simultaneous images of the global north polar region obtained with the three FUV imagers may be combined to derive the instantaneous spatial distribution of the flux of precipitating electrons and their mean electron energy. These average energies and fluxes derived by inverting FUV data are validated in a comparison with simultaneous in situ measurements with the TED particle detectors on board NOAA-16. The method is then applied to the analysis of the development of a substorm which occurred on 28 October 2000. The magnetic local time variation of the latitudinally integrated precipitated fluxes of electrons and their mean energy is displayed in keograms showing the time evolution of the precipitated flux and the mean energy of the auroral electrons. Similarly, the latitudinal distribution of these quantities in selected local time sectors is described in the course of the substorm. Based on these MLT and MLAT keograms, we describe the characteristics of the incident electron energy in comparison with the morphology and time development of the electron precipitation during the substorm. A FAST crossing of the auroral oval in the 1900 MLT sector illustrates that the combination of global UV imaging and in situ measurements of the directional electron precipitation provides a powerful tool to analyze physical process implicated in substorms.

2. FUV Imagers

[6] The IMAGE satellite was launched in March 2000 to investigate the response of the magnetosphere to the time variable solar wind [*Burch et al.*, 2001]. It is in a highly elliptical orbit with an initial perigee altitude of 1000 km and an apogee altitude of about 7 Earth radii. The FUV instrument includes three imagers which observe the global north aurora [*Mende et al.*, 2000]. The Wideband Imaging Camera (WIC) imager has a passband between 140 and 180 nm. It is mostly sensitive to the LBH bands and the NI 149.3 nm line but also includes a small contribution from the OI 135.6 nm and NI 174.3 nm lines. Excitation of the LBH bands and NI lines is produced by incident primary electrons, protons and secondary electrons colliding with N_2 molecules. The WIC CCD camera outputs the information digitally in the form of 8-bit AD units. From apogee, each WIC pixel intercepts a 70×70 km^2 square projected on the Earth. The Spectrographic Imager (SI) is a two-channel narrow-band imager of the auroral emissions at 121.8 nm and 135.6 nm. SI12 images the brightness of Doppler shifted Lyman-α auroral emissions. As precipitating protons collide with neutral atmospheric constituents they can capture an electron and become fast hydrogen atoms. A fraction of the fast H atoms are produced in the H(2p) state and radiate Doppler-shifted Lyman-α photons. SI12 efficiently rejects the geocoronal Lyman-α emission at 121.59 nm and only responds to proton precipitation [*Mende et al.*, 2001; *Gérard et al.*, 2001]. An important feature of IMAGE-FUV is the simultaneity of the multispectral imaging and its ability to discriminate proton and electron aurora. SI13, the second spectral imager, is centered on 135.6 nm with a 5 nm wide passband. This window includes the OI 135.6 nm doublet and a few adjacent LBH bands. Detailed modeling has shown that the 135.6 nm emission contributes 40–60% of the SI13 count rate, depending on the particle energy [*Hubert et al.*, 2002]. A snapshot of the global north auroral emission is obtained simultaneously by the three imagers every 121 s. The effective exposure time is approximately 10 s for WIC and 5 s for both SI12 and SI13. Performances of the FUV imagers (field of view, point spread function, and absolute sensitivity) were determined by in-flight observation of hot stars of known spectral brightness [*Gladstone et al.*, 2000; *Frey et al.*, 2002]. The overall sensitivity of each imager is controlled daily by monitoring their response to hot stars repeatedly crossing the field of view of the cameras.

3. Methodology

3.1. Principles

[7] A series of steps are needed to convert raw count rates into physical units (kiloRayleighs, mW/m^2, keV) and also to retrieve the auroral electron characteristics from global FUV imaging. They include background count subtraction, corrections for line of sight and atmospheric absorption and application of the instrumental response to sources of known absolute brightness. The conversion of the corrected count rates into absolute FUV emission rates and incident energy flux is based on simulations with models which calculate their energy degradation in the atmosphere and the subsequent emission of FUV photons. For this purpose, we use the electron and proton transport models described by *Hubert et al.* [2001]. Once the column emission rate is calculated for a given precipitation, the spectral brightness emerging from the atmosphere is multiplied by the instrumental response to determine the count rate expected for a unit incident flux in the WIC and SI13 images [*Coumans et al.*, 2002; *Hubert et al.*, 2002].

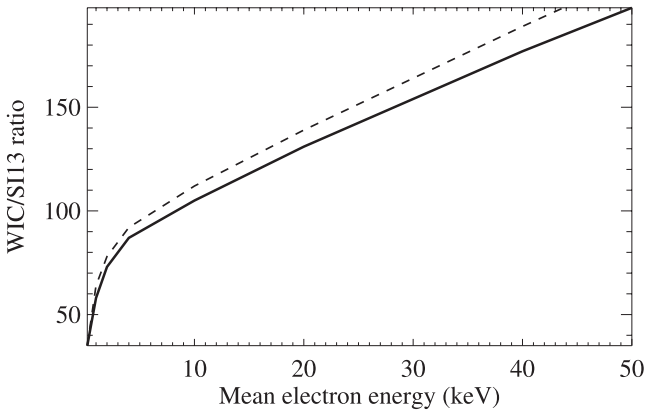

Figure 1. Calculated variation of the WIC/SI13 ratio with the electron mean energy for the MSIS atmosphere and nadir viewing (solid line). The dashed line is the same curve for a O/N_2 ratio decreased by 30 percent (see text).

[8] The calculation of the emissions expected for a given precipitated electron flux is based on the GLOW model [*Solomon et al.*, 1988]. A Maxwellian distribution is adopted to describe the differential electron energy distribution at the top of the atmosphere [*Strickland et al.*, 1993]:

$$f(E) = \frac{Q_0}{2\pi E_0^2}\frac{E}{E_0}\exp\left(-\frac{E}{E_0}\right)$$

where E_0 is the characteristic energy of the electrons, Q_0 is the total energy flux (mW/m^2), and $\langle E\rangle = 2E_0$ is the mean electron energy. Absorption by O_2 is taken into account to calculate the apparent emission rate observed from space for a defined viewing geometry.

[9] Emission due to proton precipitation is calculated using a Monte Carlo method [*Gérard et al.*, 2000] with a kappa approximation for the proton energy distribution:

$$f(E) = \frac{Q_0}{2\pi E_0^2}\frac{(\kappa-1)(\kappa-2)}{\kappa^2}\frac{E}{E_0}\frac{(\kappa E_0)^{\kappa+1}}{(E+\kappa E_0)^{\kappa+1}}$$

where E_0 is the characteristic energy of the protons and Q_0 is the total energy flux. For the kappa approximation, $\langle E\rangle = 2E_0\frac{\kappa}{\kappa-2}$ is the mean proton energy. The kappa index κ used in this study is 3.5, since it provides a good fit to averaged measured proton distributions [*Hubert et al.*, 2001]. Atmospheric absorption is generally small for the range of energies usually encountered for auroral protons [*Hubert et al.*, 2001]. As for the electrons, the count rate associated with a given incident proton spectrum is calculated for the three imagers. For SI12, it results from the direct interaction of the proton beam with the atmosphere. For WIC and SI13, the LBH, NI, and OI 135.6 nm emissions are excited by the secondary electrons resulting from ionization by the energetic protons.

[10] The WIC/SI13 ratio is an indicator of the electron mean energy. Since both instruments operate at different wavelengths, the effect of O_2 absorption is different for photons observed with the two imagers. The average electron energy, which controls the penetration depth of the electrons, affects the WIC and SI13 signals differently. In addition, the WIC/SI13 ratio bears the signature of the decreasing O/N_2 ratio when more energetic electrons penetrate deeper into the atmosphere. The ratio of these curves increases with electron energy, reflecting both the change of the differential optical thickness and the variation of the atmospheric composition with altitude. The calculated variation of the WIC/SI13 ratio with the mean electron energy is shown in Figure 1 for vertical viewing. The calculation of the distribution of electron mean energy in the aurora requires several steps.

[11] 1. Some treatment must be applied to the WIC and SI13 data to account for the different fields of view, optical distortion and integration times of the imagers. The size of the images is 256 × 256 pixels for WIC and 128 × 128 pixels for SI. We first map the SI image into the WIC image space. This procedure also includes flatfield corrections and pixel coregistration so that each corresponding pixel in WIC, SI12, and SI13 represents the same field of view.

[12] 2. Background subtraction. This step is performed by a statistical method based on the brightness histogram of the image. The present study is limited to the night side of the polar region so that no airglow correction is required.

[13] 3. The WIC and SI13 images are smoothed to reduce the statistical noise of each pixel and mapping errors (on the order of 1 or 2 pixels).

[14] 4. WIC and SI13 images may include a proton contribution. Therefore the final step before extracting the electron mean energy is the subtraction of the proton-induced signal in WIC and SI13 images. Figure 2 shows the efficiency of the WIC and SI12 imagers to the incident proton characteristic energy for a unit precipitated energy flux. They were calculated with the electron and proton

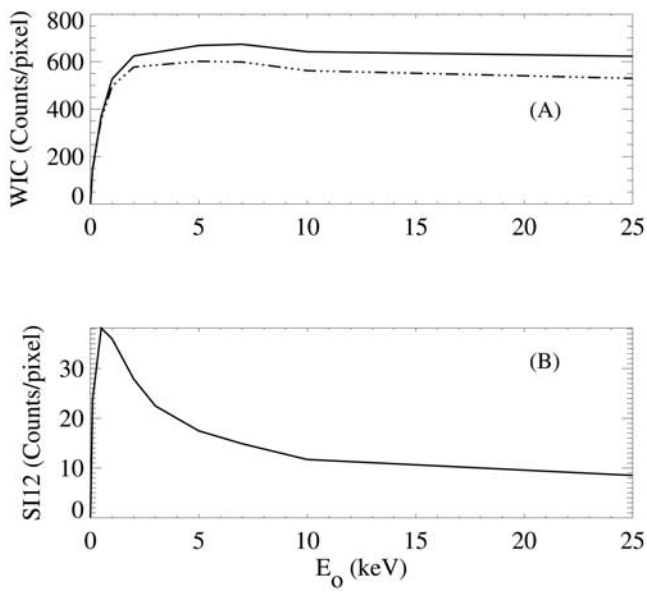

Figure 2. (a) Efficiency of the WIC camera (in count pix^{-1}/incident mW m^{-2}) as a function of the proton characteristic energy E_0 for a kappa energy distribution. The solid line is for a standard MSIS atmosphere (see text) without O_2 absorption. The dashed line is the efficiency curve when O_2 absorption is considered. (b) SI12 count rate as a function of the proton characteristic energy (in count pix^{-1}/incident mW/m^{-2}).

transport model described before. The subtraction of the proton contribution uses the corresponding SI12 image and an assumption concerning the proton energy. Assuming a kappa distribution, the proton flux may be deduced from the model SI12 efficiency (Figure 2) for the appropriate viewing geometry. The number of WIC and SI13 counts due to protons is then determined for each pixel based on calculations of the proton-induced N_2 LBH and OI 135.6 nm emissions [*Frey et al.*, 2001; *Hubert et al.*, 2001; *Coumans et al.*, 2002] and subtracted from the two images.

[15] 5. The corrected ratio of the WIC to SI13 counts due to auroral electrons is then calculated for each pixel. A ratio image is generated which may be quantitatively interpreted in terms of electron mean energy with the curve of Figure 1. Using the electron mean energy and the corrected WIC number counts for each pixel, electron efficiency curves from *Hubert et al.* [2002] are used to deduce the local electron energy flux.

3.2. Sensitivity to the Neutral Atmosphere

[16] The background atmosphere used for the efficiency calculation was obtained from the MSIS-90 model [*Hedin*, 1991]. The MSIS parameters are the conditions of a day during a solar maximum activity (24 December 1989) characterized by F10.7A = 216, F10.7 = 205, latitude = 65°, and a geomagnetic index Ap = 6. The F10.7 solar activity index is similar to the values which prevailed during the observations reported in the study (224 and 182) so that these conditions are adopted as a standard atmosphere for the efficiency curves described before. The absorption properties depend on the atmospheric composition. In particular, the ratio of the vertical column of atomic oxygen above 120 km to the column of N_2 varies with the level of auroral activity. Our standard model is characterized by a O/N_2 column ratio above 120 km of 0.52.

[17] Although the ratio of the WIC to the SI13 response mainly depends on the electron energy, it also reflects to some extent changes in the atmospheric chemical composition. *Hecht et al.* [2000] reported local perturbations of the O/N_2 density ratio up to a factor of 2, probably due to vertical upwelling of molecular rich gas generated by auroral heating. It is thus important to estimate the contribution of O/N_2 variation on the electron mean energy deduction. Bright auroral arcs fill only a small portion of the FUV field of view. Such large localized upwellings would not substantially perturb the mean composition in an area as large as the area subtended by the FUV point spread function. Consequently, as a sensitivity test, a drop by 30% of the O/N_2 column ratio above 120 km (from 0.52 to 0.37) is applied to assess the influence of composition perturbations on the mean energy determination. Since the origin of this variation is mainly upwelling of molecular richer gas, only a decrease of the O/N_2 ratio is simulated here. A second WIC/SI13 ratio curve is generated for comparison with the standard atmsophere (dashed line in Figure 1). It is seen, for example, that a drop by 30% of the O/N_2 ratio integrated on the column above 120 km causes a variation of 16% in the derived mean electron energy for an observed ratio of 120. In the same way, a drop by 29% of the O/N_2 ratio at 130 km imply a variation of 16% in the derived mean energy. This result is in good agreement with *Germany et al.* [1990] curves which show that a variation of 35% of the O/N_2 ratio at 130 km imply a variation of 11% for a fixed ratio OI 1356/LBH 1838.

4. Validation With In Situ Measurements

[18] We now compare the characteristics of the auroral electron energy spectra derived from the set of FUV images with simultaneous in situ measurements. The validation of the electron mean energy and energy flux deduced from FUV data is made with the Total Energy Detector (TED) experiment on board the NOAA-TIROS 16 satellite. TED measures the directional energy flux carried towards the atmosphere by electrons and positive ions in the energy range from 50 eV to 20 keV. The measurements are made at two angles from the vertical (0° and 30°). Particles with these pitch angles are within the atmospheric loss cone in the auroral regions. The sixteen logarithmically spaced NOAA-16 energy channels are listed by *Coumans et al.* [2002].

[19] Every 8 s, the directional particle energy fluxes contained in energy bands 4, 8, 11, and 14 are determined for electrons and protons by the two detectors. The directional particle energy flux contained in the energy band identified as containing the maximum flux of any of the 16 energy bands and the energy band number containing the maximum in the flux are also available. Modeling of the instrument response shows that the center of the maximum flux channel is generally where the maximum of the differential energy spectrum occurs [*Fuller-Rowell and Evans*, 1987]. We assume that this distribution is Maxwellian so that this energy is also the mean electron energy $2E_o$.

[20] For this comparison, we extracted the instrumental count rate for the FUV pixel corresponding to the footprint of the magnetic field line at the instantaneous NOAA spacecraft position. A FUV image is obtained every 2 min. Therefore out of each individual FUV image, the FUV count rate was extracted along the footprint track of NOAA-16 from the position 1 min before to 1 min after the central snapshot time. A basic limitation concerns short-lived features occurring between two FUV snapshots. Such features are detected by NOAA but would be invisible to FUV. A second limitation is the difference of spatial resolution between the two data sets. The spatial resolution of the in situ data is much higher than the FUV instrumental resolution as discussed by *Gérard et al.* [2001] and *Coumans et al.* [2002].

[21] To account for this difference, it is necessary to smooth the NOAA data before comparing the particle count rate with the FUV signal. The amount of smoothing to be applied to the NOAA measurements is determined by the number of NOAA data point corresponding to the imagers' point spread finction (PSF). From apogee, a WIC pixel projects as a $\sim 70 \times 70$ km^2 square on Earth. In terms of geocentric angles, 70 km correspond to 0.63°. To account for the WIC PSF we smooth over 1.5 FWHM ($\sim$6 pixels) [*Coumans et al.*, 2002], i.e., a width corresponding to a drop of 66% of the peak of the Gaussian PSF. These six pixels are equivalent to a geocentric angle of 3.8°. The NOAA satellite moves by 3.8° in $\sim$66 s; therefore the NOAA data are smoothed over four consecutive data points. Another source of difference in the effective spatial resolution stems from the fact that the FUV signal in each pixel includes

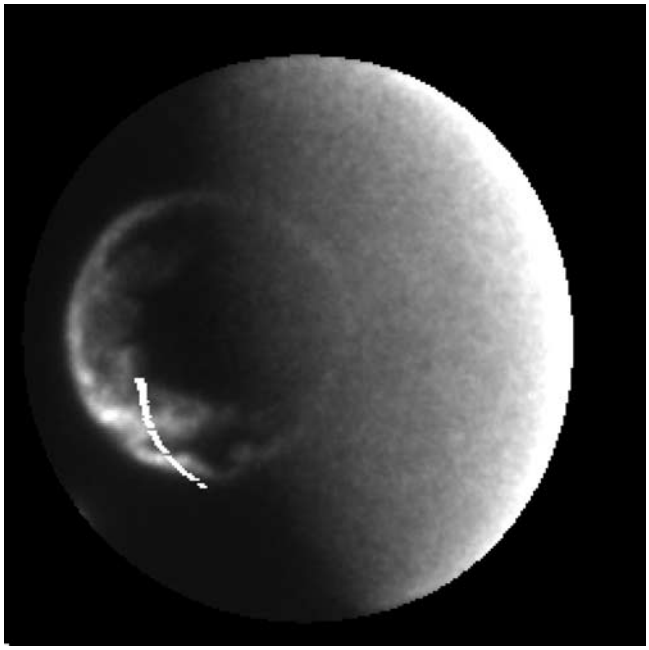

Figure 3. WIC image of the North polar region obtained on 21 October 2001 at 1727 UT. The white segment shows the track of the NOAA 16 orbit projected at 120 km. The spacecraft moved equatorward across the auroral oval. See color version of this figure at back of this issue.

emission contributions from adjacent lateral regions not probed by the NOAA detector.

4.1. First Case Study

[22] We first describe a FUV-NOAA comparison from a NOAA-16 over flight which occurred on 21 October 2001 (day 294) between 1727 and 1731 UT. This period was a part of substorm which started at 1656 UT and was preceeded by moderate auroral and magnetic activities (Kp = 2). The first onset was located in the premidnight sector. About 18 min later (1714 UT) particle injection occurred in the postmidnight sector and expanded both in magnetic latitude (MLAT) and magnetic local time (MLT). The period of over flight took place during the expansion of this second phase, when Kp reached a level of 6. The track of NOAA-16 satellite orbit is shown in Figure 3, together with the WIC image obtained at 1727 UT. The NOAA satellite moves nearly parallel to the terminator. The auroral crossing occurred entirely in the nightside sector.

[23] Figure 4 presents the result of the comparison between NOAA-TED and IMAGE-FUV quantities for an assumed proton kappa distribution with a mean energy of 2 and 8 keV. The thick dark solid line represents FUV-derived values for the 8-keV assumption on the proton mean energy, while the thick dark dotted line shows the FUV-derived values in the 2-keV assumption. These two curves illustrate the sensitivity of the FUV-derived quantities to the proton mean energy. The two curves are slightly different but the quantitative and morphological features are very similar. Error bars on the thick dark solid line represent the uncertainty on the electron mean energy due to statistics on the count rates of the WIC and SI13 cameras. The red-dotted line represents the average between the 0° and 30° NOAA data and the dashed-dotted line the proton energy flux. The global features observed by NOAA are well reproduced by FUV, both for mean energy and energy flux. The inverted FUV data underestimate the electron mean energy (top panel) near 1727:30. This energy peak corresponds to a region of low flux ($\simeq$1.5 mW/m^2) where the NOAA mean energy determination is less reliable. For both the first and the second peak, NOAA and FUV values are remarkably close. The two electron energy peaks are colocated with the maxima of the energy flux and may be identified with the crossings of the NOAA track with two bright auroral regions seen in Figure 3. The peak flux values

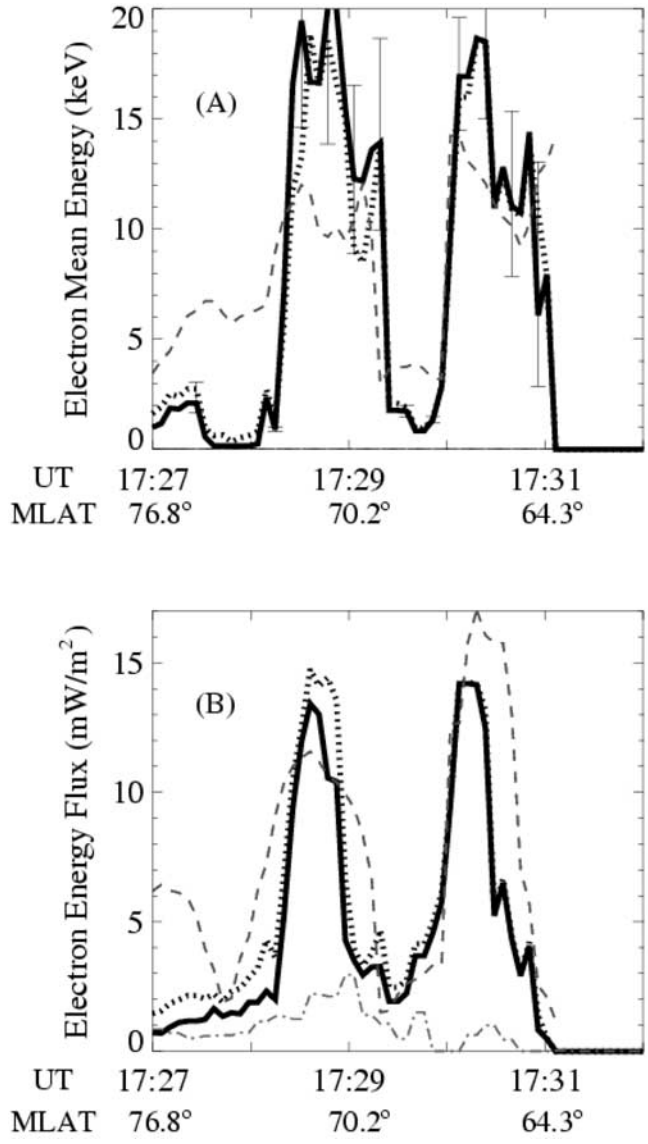

Figure 4. Distribution of the mean electron energy (a) and energy flux (b) deduced from simultaneous WIC, SI12, and SI13 images on 21 October 2001 (as shown in Figure 3). The dark thick solid line is for a 8 keV mean proton energy; the dark thick dotted line is for 2 keV. For comparison, simultaneous in situ measurements from a NOAA 16 overflight are also shown (red curves). The proton energy flux measured by the NOAA particle detector multiplied by 5 is also shown in Figure 4b (blue curve). See color version of this figure at back of this issue.

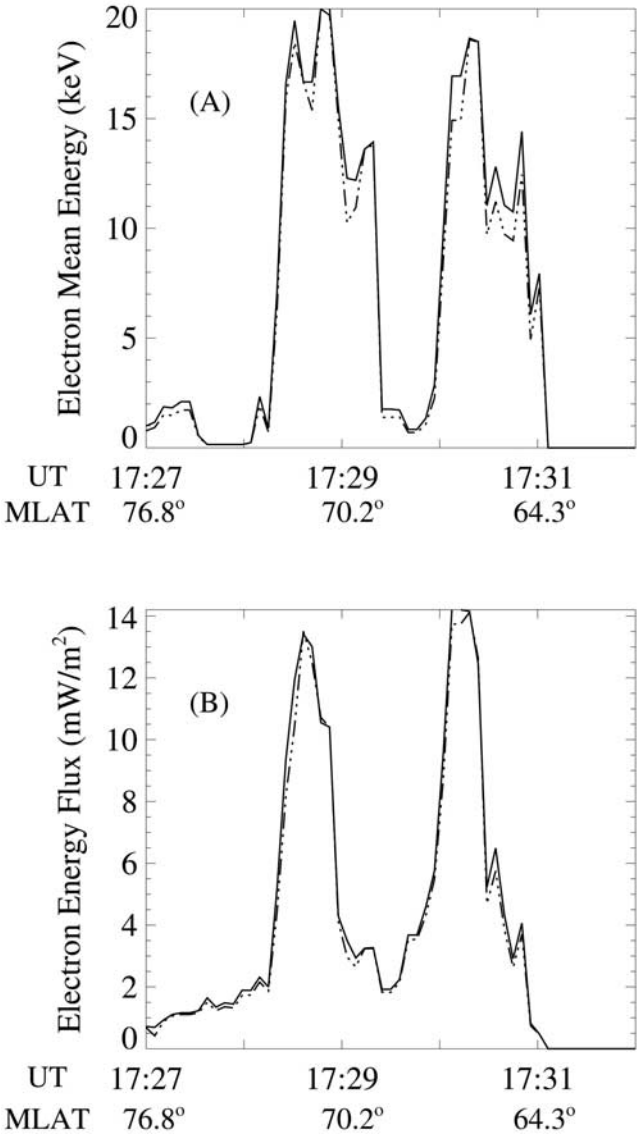

Figure 5. Electron mean energy (a) and electron energy flux (b) deduced from simultaneous FUV images with the three cameras. The solid line shows the values obtained for the MSIS atmosphere. The dashed line is for a perturbed atmosphere with a O/N_2 ratio decreased by 30 percent.

(bottom) are within 17% of the in situ measurements. The plots indicate that the regions with higher fluxes show best agreement between FUV and NOAA values.

[24] The comparisons of FUV and NOAA are good for the assumption of a proton mean energy between 2 and 8 keV (i.e., E_0 between 0.4 and 1.7 keV). For proton mean energies greater than about 10 keV (i.e., E_0 = 2.1 keV), the comparisons deteriorate (not shown). This result can be explained based on the SI12 and WIC efficiency curves. The determination of the electron mean energy is unrealistic if a too high proton mean energy is assumed since the SI12 efficiencies severely decrease at high energy (Figure 2), causing an overestimate of the proton flux and the subtracted WIC counts. Consequently, the WIC/SI13 ratio and the apparent electron mean energy both decrease. Since the electron energy flux determination is based on the corrected WIC count, the electron flux so determined will be underestimated.

[25] The relationship between the WIC/SI13 ratio and the mean electron energy depends to some extent on atmosphere composition. The electron mean energy and electron energy flux deduced from IMAGE data with the standard and perturbed atmospheres described before are compared in Figure 5. The atmosphere perturbation implies at most a 15% variation of the deduced electron mean energy.

4.2. Second Case Study

[26] This second overflight used for this validation occurred from 1911 to 1915 UT, 2 hours later than case 1, when Kp = 6. The emission presents no specific structure and was approximately 7° degrees of latitude wide and fairly homogeneous around the midnight sector. During the NOAA-16 satellite crossing, the auroral structure was stable in space and time. For this comparison, we assumed a 8 keV proton energy. As before, the result is fairly insensitive to the choice of a proton energy in the range 1–10 keV. Figure 6 illustrates

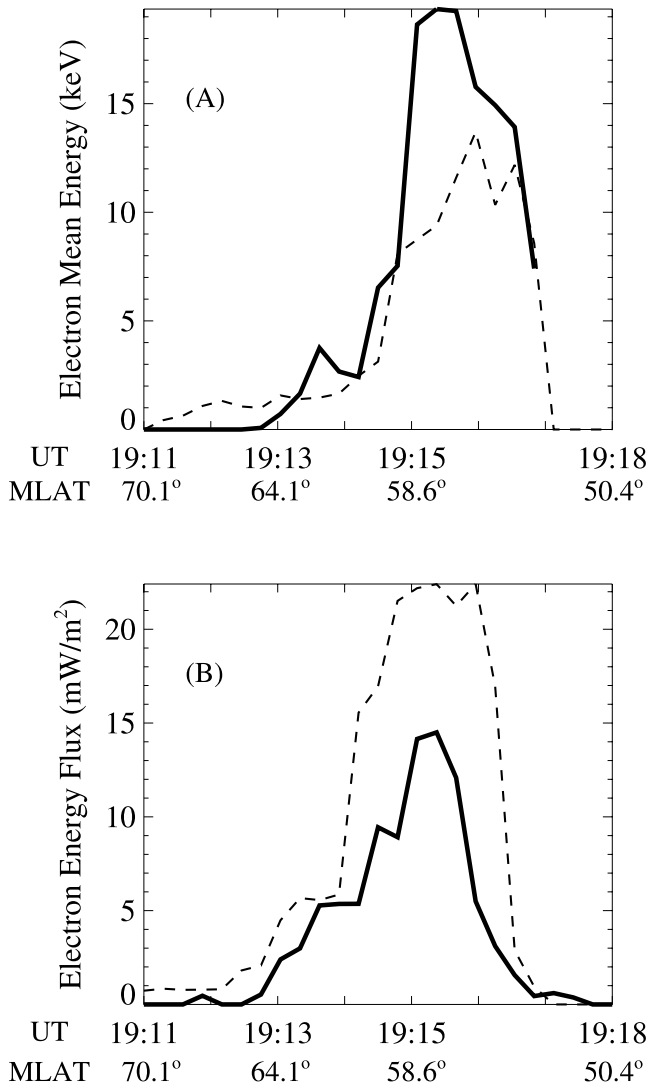

Figure 6. NOAA 16 crossing of the auroral oval on the same day (21 October 2001, not shown in Figure 3) from 1911 to 1918 UT. Solid lines represent electron mean energy (a) and energy flux (b) deduced from FUV images. The dashed lines show simultaneous in situ NOAA particle data.

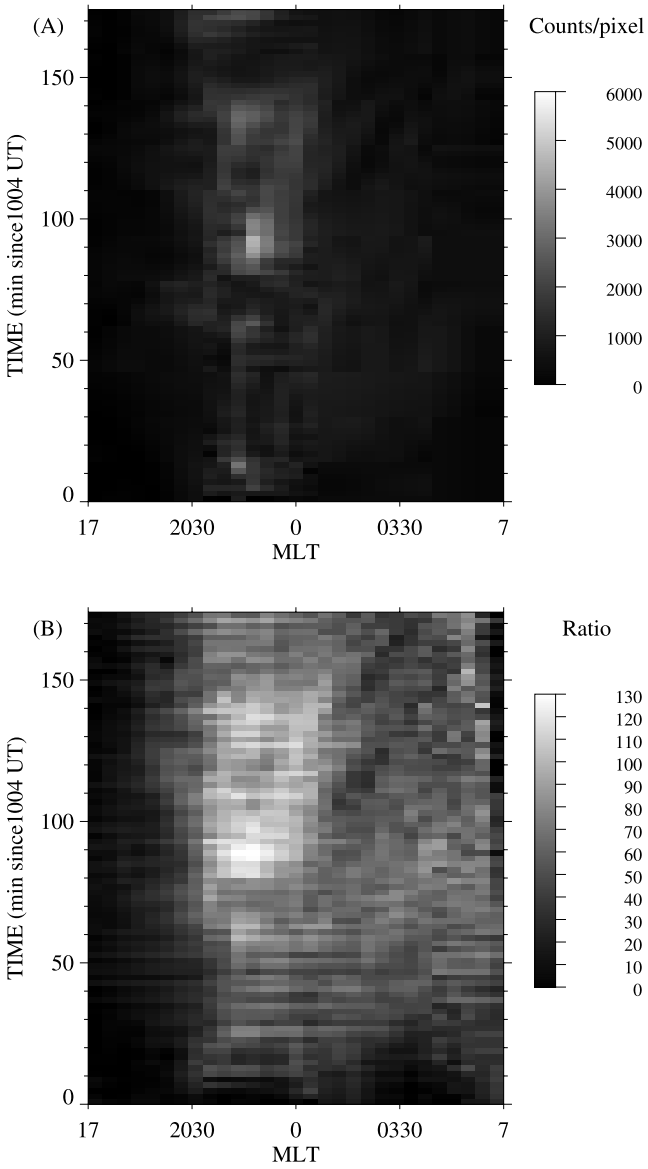

Figure 7. FUV data showing the magnetic local time distribution of two auroral substorms observed with IMAGE-FUV (on 28 October 2000 from 1004 to 1300 UT). (a) WIC counts and (b) corrected WIC/SI13 ratio. All pixels exceeding the scale upper limits are shown in white. See color version of this figure at back of this issue.

the comparison of the mean electron energy and the precipitated energy flux determined from the two satellites.

[27] The global morphology of the electron mean energy is very well reproduced. The energy maximum values from FUV and NOAA are similar, although the FUV peak values overestimate the NOAA values by 45%. The flux morphology is well represented by the FUV observations, although the NOAA curve is narrower than the FUV distribution. The peak values deduced from FUV are less by 35% than the in situ data.

5. Substorm Energetics and Dynamics

[28] To illustrate the potential of the method described in section 3.1 to determine the electron flux mean energy, we introduce color-coded keograms summarizing the time evolution of auroral activity which occurred on 28 October 2000 (day 302) between 1000 and 1300 UT. All data are displayed as a function of the magnetic local time (MLT) and UT (Figures 7 and 8) or magnetic latitude (MLAT) and UT (Figures 9 and 10). The evolution of the substorm in UT is shown in terms of WIC counts, WIC/SI13 ratio, electron energy flux (mW/m^2) and mean electron energy (keV). The values are based on the combination of the WIC, SI12 and SI13 sequences of images processed with the method previously described. A given set of three images (for a given time) corresponds to a horizontal line of the diagram of Figures 7 and 8 and to a vertical line of the Figures 9 and 10.

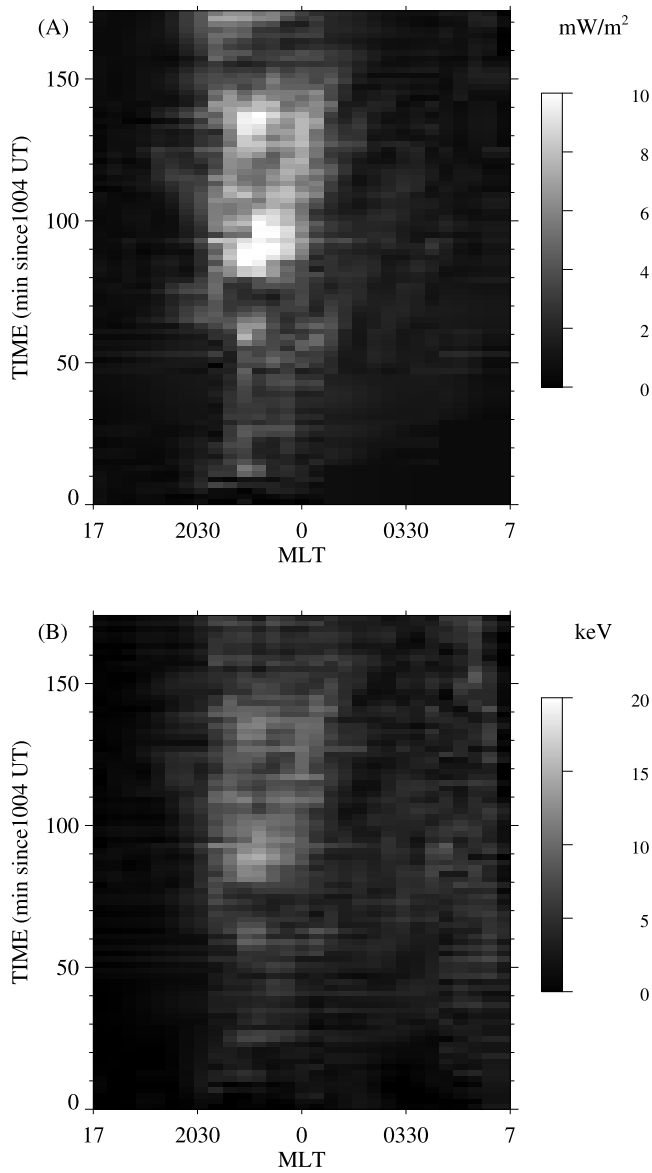

Figure 8. Characterization of the evolution of the electron precipitation during substorms deduced from FUV data. The two auroral substorms are the same as in Figure 7. (a) Precipitated electron energy flux (mW/m^2) and (b) mean electron energy (keV). Pixels with values exceeding the scale upper limits are shown in white. See color version of this figure at back of this issue.

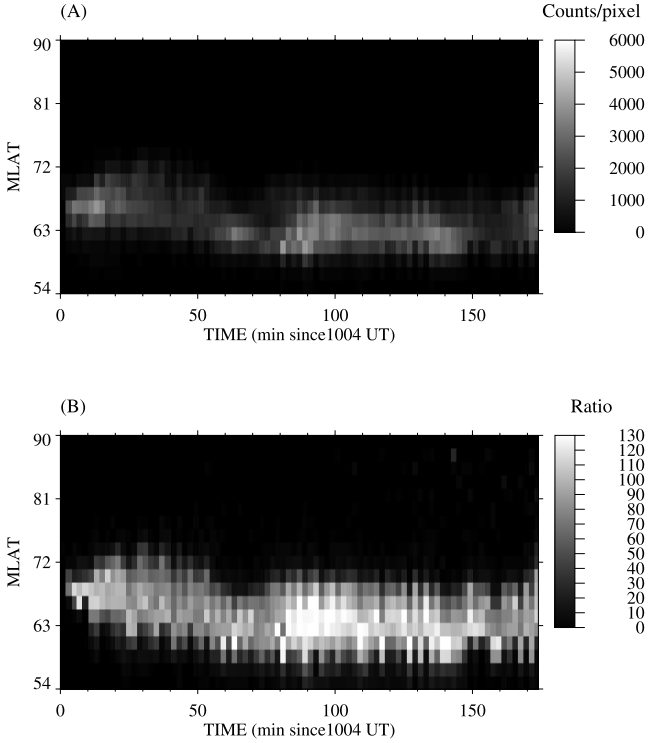

Figure 9. FUV data showing the magnetic latitudinal distribution of the two auroral substorms (28 October 2000 from 1004 to 1300 UT) in the 2100–2400 MLT sector. (a) WIC counts and (B) corrected WIC/SI13 ratio. Pixels with values exceeding the scale upper limits are shown in white. See color version of this figure at back of this issue.

Each 2 min time step, all pixels between 58° and 68° MLAT are summed up and the resulting MLT variation is binned into 30 min MLT sectors. All pixels in each MLT bin are averaged and the resulting value is set to the corresponding pixel in the diagram. The procedure is the same with all four displays. No airglow correction was applied to the dayside data. Consequently, dayside MLT sectors (0700 to 1700 MLT) will be ignored.

[29] The activity period described in Figures 7, 8, 9, and 10 occurred on 28 October 2000. It includes two injections and one additional onset. The magnetic activity before the first injection was very weak but increased considerably during the substorm when the Kp index reached 6. The cause of the first onset may be related to the solar wind conditions measured by the Advanced Composition Explorer (ACE) satellite and shown in Figure 11. A few minutes after 0900 UT (this time corresponds to a few minutes after 1004 in the keograms), a sharp increase of the bulk speed and proton density of the solar wind was observed. At this time the B_z component decreased from a value close to zero to about -10 nT.

[30] The corresponding auroral substorm onset (the first injection) was located in the premidnight sector. The associated electron energy is ~10 keV and the flux is about 8 mW/m^2. The electron mean energy remains roughly constant until the second electron injection. Following the onset, the electron energy flux decreased to ~5 mW/m^2. The highest electron energies are primarily located in the 2200–0000 MLT sector. During the first 20 min, the highest energy injection progressively widens and slightly drifts toward the midnight MLT meridian. Subsequently, the location of the highest energy injection remains constant in MLT. The energy flux shows the same structure as the mean energy. However, parallel bands of bright structures of enhanced flux and mean energy are observed drifting from the midnight to the morning sector between 1020 and 1130 UT. This eastward drift is also seen on the WIC count diagram. These features correspond to precipitation of electrons with energies less than 7 keV carrying a flux of 2–3 mW/m^2. They move eastward with a speed of ~5 MLT hours/UT hour that is nearly 5 times the corotation velocity. At auroral latitudes, this value corresponds to a projected speed of nearly 1200 m/s. Such movements and speed were already observed by *Meinel and Schulte* [1953] and *Davis* [1967].

[31] If caused by an eastward $\mathbf{E} \times \mathbf{B}$ drift, the value of the electric field may be derived from the drift velocity of 1.2 km/s. For an electron energy of 5 keV (Figure 8) the gradient curvature drift acounts for 0.15 km/s, and hence an additional 1 km/s may be due to a southward E field. At 120 km, it corresponds to a southward directed electric field of about 54 mV/m. This eastward motion is not clearly identifiable as a discrete feature in the sequence of FUV images. Rather, it corresponds to a motion of the latitudinally integrated amount of auroral emission. Eastward

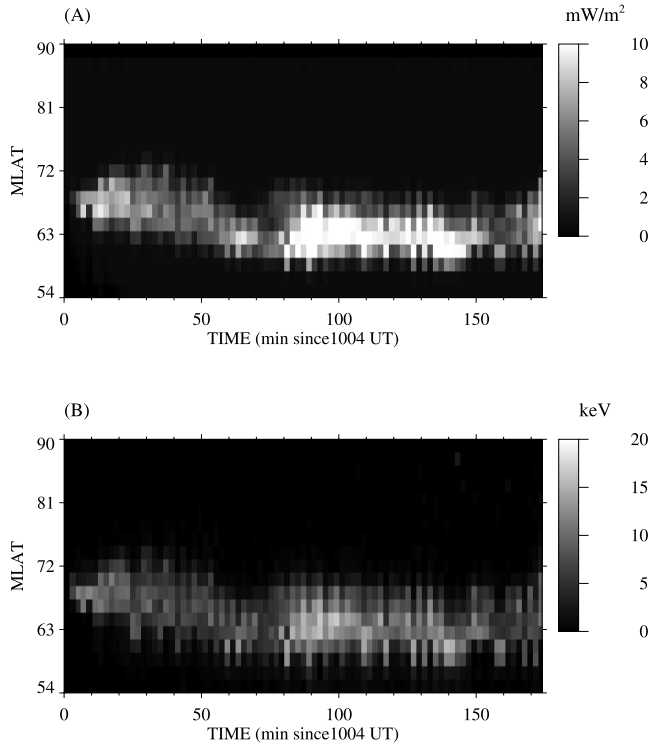

Figure 10. Characterization of the latitudinal distribution of the electron precipitation during auroral substorms deduced from FUV data. The two auroral substorms are the same as in Figure 9. The 2100–2400 MLT sector is illustrated here. (a) Electron energy flux (mW/m^2) and (b) mean electron energy (keV). See color version of this figure at back of this issue.

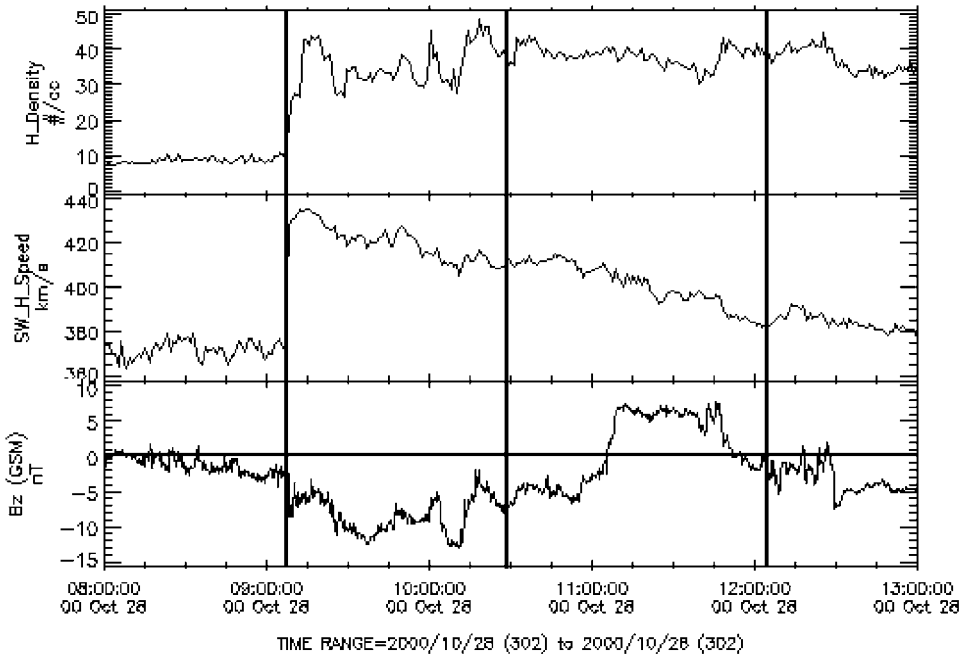

Figure 11. Solar wind characteristics measured at the L1 Lagrangian point by the ACE satellite (28 October 2000). (top to bottom) Solar wind proton density (cm^{-3}), bulk velocity (km s^{-1}), and B_z IMF component. The vertical bars show the shifted times of the substorm onsets observed with FUV.

travelling motion of large magnetic perturbations were previously observed from the ground [*Kawasaki and Rostoker*, 1979] at magnetic latitudes between 60° and 70°N. The speeds measured in the nonrotating frame of reference ranged from 0.8 to 2.1 km/s.

[32] Just preceeding the second injection, the maximum flux and energy move to the evening sector and remain near 2000 MLT for about 15 minutes. Figures 9 and 10 show the corresponding keogram in MLAT-UT coordinates for the premidnight sector (2100–2400 UT) where the substorm initially develops. Variations observed in the WIC/SI13 ratio indicate that the characteristic energy of the precipitated electrons exhibits temporal and latitudinal variations. Electron energies on the order of 12 keV are associated with the 20 min following the onset, followed 50 minutes later by a gradual drop to about 7 keV. The WIC signal and the energy flux show an initial broadening of the oval both poleward and equatorward. It is followed by a continuous equatorward motion by about 4° of MLAT from 30 to 60 min after onset. This phase is followed by a short lived intensification without latitudinal drift preceeding the second substorm onset.

[33] A few minutes before the second injection seen in Figures 7 and 8, the FAST [*Carlson et al.*, 1998] satellite crossed the auroral oval (Figure 12). Around 1120 UT the FAST satellite penetrated into a precipitation region poleward of and slightly detached from the main oval. This region intensified 7 min earlier and the intensity slowly increased until 1122 UT. It subsequently decreased and moved toward midnight. The FAST spectrograms (Figure 13) display the signature of two types of precipitation. Between 1120:15 UT and 1120:30 UT, a superthermal injection characterized by a broad spectral enhancement and a collimated beam along the magnetic field lines is observed. These features are usually interpreted as electrons accelerated by wave particle interaction [*Burch*, 1991]. The energy flux and number flux are large with a low electron mean energy and a pitch angle distribution strongly peaked downward. At 1121 UT, a second type of precipitation is observed. The pitch angle distribution is almost isotropic and precipitation features exhibit a high energy and rela-

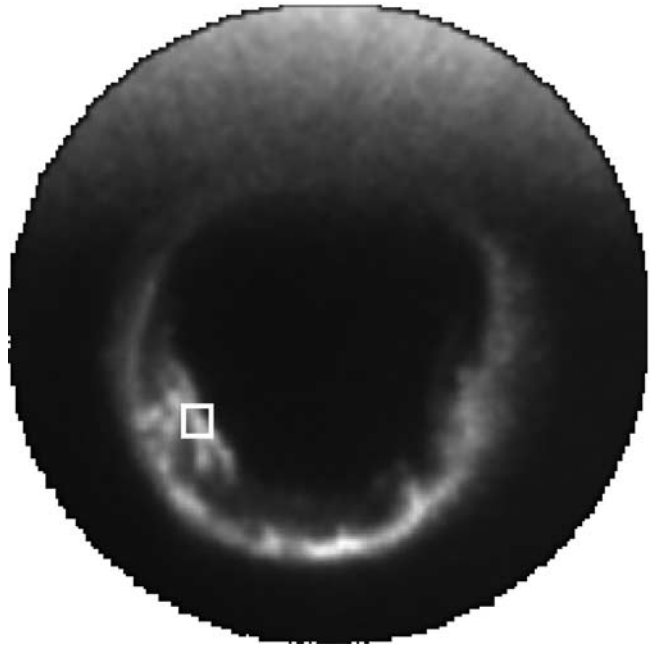

Figure 12. Location of the FAST crossing of the oval shown on the WIC image (28 October 2000) at 1120 UT. See color version of this figure at back of this issue.

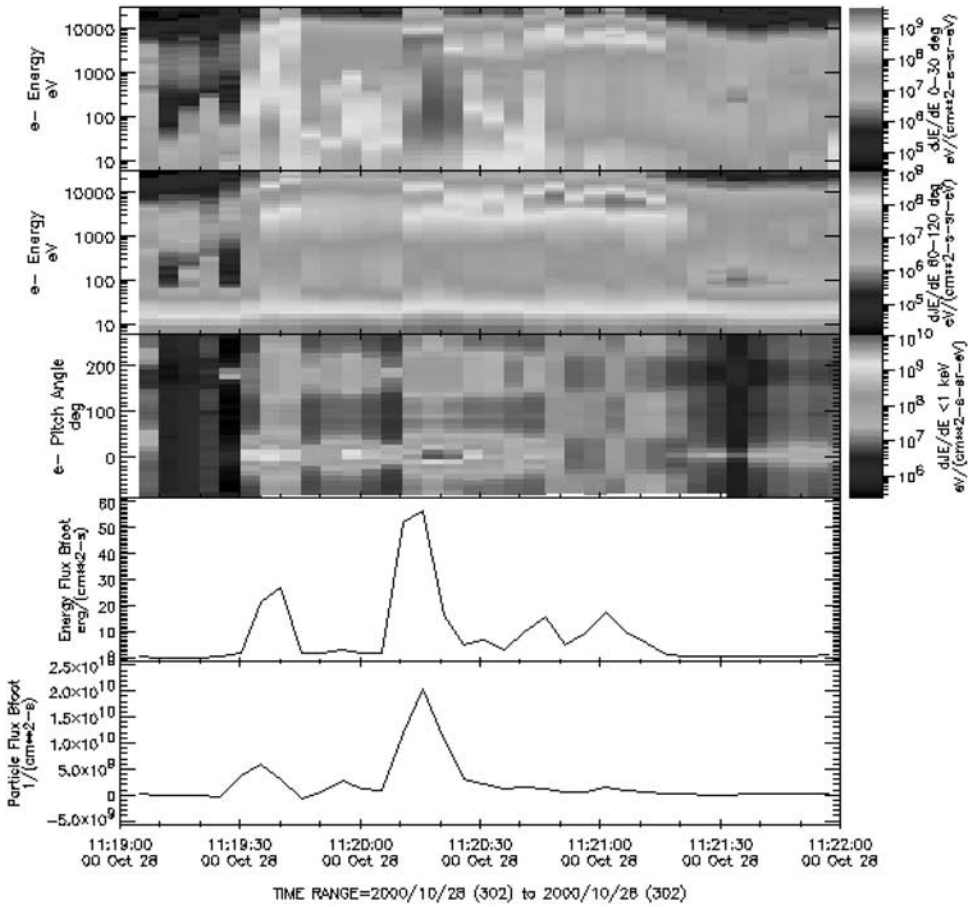

Figure 13. (top to bottom) The electron energy spectrograms, with pitch angles between 0° and 30°, 60°, and 120°, the pitch angle distribution, the energy and the number flux. See color version of this figure at back of this issue.

tively monoenergetic peak at ~9 keV. This type of precipitation is consistent with quasi-static potential structures [*Ergun et al.*, 1998; *McFadden et al.*, 1999]. This precipitation zone is seen in the keogram presented in Figure 14. A narrow MLAT band ranging between 69° and 72° is represented in the keogram for all MLTs. The region of the emission crossed by FAST is located in the 1900 MLT sector, 76 min after the start of the keogram (1004 UT). This keogram shows the beginning of this emission around 1110 UT, an intensification until 1122 UT, and final decrease. The drift motion to the midnight sector is clearly visible between 1110 UT and 1134 UT. However, the FUV imagers are not able to discriminate between two types of acceleration processes. For example no region of lower WIC/SI13 ratio (low electron energy) is observed poleward of an area of higher ratio (high electron energy) as would be expected from the changes of electron energy seen in Figure 13 between 1120 and 1121 UT. This insensitivity is a consequence of the spatial intergration over the FUV PSF which prevents structures finer than ~100 km to be identified.

[34] The second injection occurred at 1124 UT, that is, 80 min after the first one. The source of this second onset was around 1020 UT in the solar wind. However, at this time, no evidence can be observed for any major change in the solar wind parameters possibly triggering of this onset (Figure 11). The IMF B_z component is negative without any conspicuous

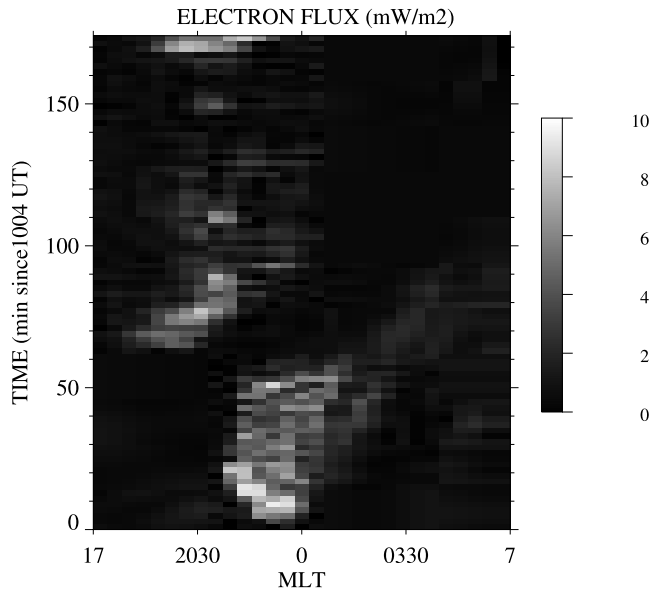

Figure 14. Electron energy flux for MLAT between 69° and 72° for the substorm of 28 October 2000 (day 302). The event observed with FAST is seen near 1900 MLT, 75 min after 1004 UT. See color version of this figure at back of this issue.

variation and the values of the solar wind speed and density remain quite smooth. The MLT keogram (Figure 8) indicates that the second electron injection was more energetic than the first one. The mean energy initially reached ~15 keV and the energy flux exceeded 10 mW/m^2. As for the first injection, the mean energy reached its peak at the same UT and MLT as the energy flux but rapidly decreased to lower value (below 10 keV). The MLT range covered by this second event is more extended and located in the 2100–0000 MLT sector. The MLAT keogram suggests a very moderate poleward motion of the bright region after 1035 UT until about 1220. The mean electron energy is generally correlated in time and colocated in MLAT with the precipitated energy. In particular, the equatorward motion of the peak electron flux following the first onset is also observed in the morphology of the mean electron energy. The highest energy values (17 keV) occur between 1130 and 1145 UT and are located slightly poleward of the center of the high electron flux region. The electron mean energy gradually decreases to about 8 keV. The most conspicuous characteristic is the similarity of the structures of average energy and energy flux as well as the localization of the high energy values in the premidnight sector. Mean electron energies in the substorm are typically around 10 keV, reaching 15 keV at the onset time. It must be stressed that these values are averaged over 0.5 hour of MLT periods. Therefore local values may well exceed these values, as observed with in situ measurements. Another feature is the fast decrease of the average energy of electrons injected after onset (~20 min), whereas the flux remains close to the onset value over nearly 1 hour. The fast variation in MLT preceding the second injection remains unexplained as well as the links between this second injection and the solar wind parameters. A third injection is visible around 1250 UT, i.e., 90 min after the second injection. It is seen in Figure 11 that a southward turning of the B_z component probably triggered this third injection.

6. Summary and Conclusions

[35] The combination of images obtained simultaneously with the three FUV imagers on board IMAGE-FUV provides a quantitative indicator of the electron mean energy and the electron energy flux. A validation of these quantities was performed by comparison with NOAA 16–TED data obtained during two NOAA auroral oval crossings. For both comparison cases the NOAA measurements are satisfactorily reproduced (within about 30%) by the FUV remotely sensed precipitation characteristics if adequate time averaging is applied to the in situ data. It was shown that at the resolution of the FUV imagers, the mean energy and flux determinations do not significantly depend on the local composition of the neutral atmosphere. As an application of this methodology, the time evolution of auroral activity occurring on 28 October 2000 is displayed in the form of magnetic local time and latitude keograms. As expected, the pattern of the electron average energy distribution exhibits both spatial and temporal changes. The highest average electron energies are generally colocated in time and space with the highest electron precipitation fluxes. Dawnward motion at speeds on the order of 5 magnetic local time hours/UT hour is observed. It is possibly linked to the presence of an electric field in the postmidnight magnetosphere. It is found that these substorm representations are well suited to describe morphological features and motions occurring before or during substorms. The combination of the keograms with remotely determined electron energy and flux provides a tool for quantitative and morphological studies of substorm evolution. Additional use of SI12 images will provide a useful tool to study the time-space variation of proton precipitations. Comparison of global scale electron and proton dynamics will be possible at a time resolution of 2 min. Additional in situ measurements with FAST highlight the ability of the IMAGE-FUV keograms to represent transient local events of a substorm and the inability to identify small scale structures that may be caused by different acceleration processes.

[36] **Acknowledgments.** J. C. Gérard is supported by the Belgian Fund for Scientific Research (FNRS). V. Coumans is supported by the FRIA. This work was also supported funded by the PRODEX programme of the European Space Agency (ESA), the Belgian Fund for for Collective Fundamental Research (FRFC grant 2.4517.02), and grant RFBR 02-02-16087. The IMAGE FUV investigation was funded by NASA through SWRI subcontract NAS5-96020. We acknowledge C. Carlson at U.C. Berkeley and CDAWeb for the FAST data.

[37] Arthur Richmond thanks Manfred Rees and another reviewer for their assistance in evaluating this paper.

References

Burch, J. L., Diagnosis of auroral acceleration mechanisms by particle measurements, in *Auroral Physics*, edited by C.-I. Meng, M. J. Rycroft, and L. A. Frank, Cambridge Univ. Press, New York, 1991.

Burch, J. L., et al., Views of Earth's magnetosphere with the IMAGE satellite, *Science*, *291*, 619, 2001.

Carlson, C. W., et al., FAST observation in the downward auroral current region: Energetic upgoing electron beams, parallel potential drop, and ion heating, *Geophys. Res. Lett.*, *25*, 2017, 1998.

Chua, D., G. Parks, M. Brittnacher, W. Peria, G. Germany, J. Spann, and C. Carlson, Energy characteristics of auroral electron precipitation: A comparison of substorms and pressure pulse related auroral activity, *J. Geophys. Res.*, *106*, 5945, 2001.

Coumans, V., J. C. Gérard, B. Hubert, and D. S. Evans, Electron and proton excitation of the FUV aurora: Simultaneous IMAGE and NOAA observations, *J. Geophys. Res.*, *107*(A11), 1347, doi:10.1029/2001JA009233, 2002.

Craven, J. D., and L. A. Frank, Latitudinal motions of the aurora during substorms, *J. Geophys. Res.*, *92*, 4565, 1987.

Davis, N. T., Worldwide auroral morpholgy, in *From Aurora and Airglow*, edited by B. M. McCormac, Reinhold, New York, 1967.

Ergun, R. E., et al., FAST satellite observations of electric field structures in the auroral zone, *Geophys. Res. Lett.*, *25*, 2025, 1998.

Frey, H. U., S. B. Mende, C. W. Carlson, J.-C. Gérard, B. Hubert, J. Spann, G. R. Gladstone, and T. J. Immel, The electron and proton aurora as seen by IMAGE-FUV and FAST, *Geophys. Res. Lett.*, *28*, 1135, 2001.

Gérard, J. C., B. Hubert, D. V. Bisikalo, V. I. Shematovich, H. U. Frey, S. B. Mende, G. R. Gladstone, and C. W. Carlson, Observation of the proton aurora with IMAGE-FUV and simultaneous ion flux in situ measurements, *J. Geophys. Res.*, *106*, 28,939, 2001.

Germany, G. A., M. R. Torr, P. G. Richards, and D. G. Torr, The dependence of modeled OI 1356 and N_2 Lyman Birge Hopfield auroral emissions on the neutral atmosphere, *J. Geophys. Res.*, *95*, 7725, 1990.

Germany, G. A., et al., Remote sensing determination of auroral energy characteristics during substorm activity, *Geophys. Res. Lett.*, *24*, 995, 1997.

Gladstone, R. G., et al., Stellar calibration of the WIC and SI imagers and the GEO photometer on IMAGE/FUV, *Eos Trans. AGU*, *81*(48), Fall Meet. Suppl., Abstract SM72A-06, 2000.

Hecht, J. H., D. L. McKenzie, A. B. Christensen, D. J. Strickland, J. P. Thayer, and J. Watermann, Simultaneous observations of lower thermospheric composition change during moderate auroral activity from Kangerlussuaq and Narsarsuaq, Greenland, *J. Geophys. Res.*, *105*, 27,109, 2000.

Hedin, A. E., Extension of the MSIS thermosphere model into the middle and lower atmosphere, *J. Geophys. Res.*, *96*, 1159, 1991.

Hubert, B., J. C. Gérard, D. V. Bisikalo, V. I. Shematovich, and S. C.

Solomon, The role of proton precipitation in the excitation of auroral FUV emissions, *J. Geophys. Res.*, *106*, 21,475, 2001.

Hubert, B., J. C. Gérard, D. S. Evans, M. Meurant, S. B. Mende, H. U. Frey, and T. J. Immel, Total electron and proton energy input during auroral substorms: Remote sensing with IMAGE-FUV, *J. Geophys. Res.*, *107*(A8), 1183, doi:10.1029/2001JA009229, 2002.

Kawasaki, K., and G. Rostoker, Perturbation magnetic fields and current systems associated with eastward drifting auroral structures, *J. Geophys. Res.*, *84*, 1464, 1979.

Lummerzheim, D., M. Brittnacher, D. Evans, G. A. Germany, G. K. Parks, M. H. Rees, and J. F. Spann, High time resolution study of the hemispheric power carried by energetic electrons into the ionosphere during the May 19/20, 1996 auroral activity, *Geophys. Res. Lett.*, *24*, 987, 1997.

McFadden, J. P., C. W. Carlson, and R. E. Ergun, Microstructure of the auroral acceleration region as observed by FAST, *J. Geophys. Res.*, *104*, 14,453, 1999.

Meinel, A. B., and D. H. Schulte, A note on auroral motions, *Astrophys. J.*, *117*, 454, 1953.

Mende, S. B., et al., Far ultraviolet imaging from the IMAGE spacecraft: 1. System design, *Space Sci. Rev.*, *91*, 243, 2000.

Mende, S. B., H. U. Frey, M. Lampton, J. C. Gérard, B. Hubert, S. Fuselier, G. R. Gladstone, and J. L. Burch, Global observations of proton and electron auroras in a substorm, *Geophy. Res. Lett.*, *24*, 1139, 2001.

Meng, C. I., and K. Liou, Global auroral power as an index for geospace disturbances, *Geophys. Res. Lett.*, *29*(12), 1600, doi:10.1029/2001GL013902, 2002.

Østgaard, N., J. Stadsnes, J. Bjordal, G. A. Germany, R. R. Vondrak, G. K. Parks, S. A. Cummer, D. L. Chenette, and J. G. Pronko, Auroral electron distributions derived from combined UV and X-ray emissions, *J. Geophys. Res.*, *106*, 26,081, 2001.

Solomon, S. C., P. B. Hays, and V. Abreu, The auroral 6300 Å emission: Observation and modelling, *J. Geophys. Res.*, *93*, 9867, 1988.

Strickland, D. J., R. E. Daniell Jr., J. R. Jasperse, and B. Basu, Transport-theoretic model for the electron-proton-hydrogen atom aurora: 2. Model results, *J. Geophys. Res.*, *98*, 21,533, 1993.

D. V. Bisikalo and V. I. Shematovich, Institute of Astronomy, Russian Academy of Sciences, 48 Pjatnistkaja Street, Moscow, Russia. (bisikalo@inasan.rssi.ru; shematov@inasan.rssi.ru)

V. Coumans, B. Hubert, J.-C. Gérard, and M. Meurant, Laboratoire de Physique Atmosphérique et Planétaire, Institut d'Astrophysique et de Géophysique, 17 allée du 6 août, B-4000 Liège, Belgium. (mmeurant@ulg.ac.be; jc.gerard@ulg.ac.be; B.Hubert@ulg.ac.be; V.Coumans@ulg.ac.be)

D. S. Evans, NOAA Space Environment Center, 325 Broadway, Boulder, CO 80305, USA. (David.S.Evans@noaa.gov)

G. R. Gladstone, Southwest Research Institute, 6220 Culebra Rd., San Antonio, TX 78228-0510, USA. (randy@whistler.space.swri.edu)

S. Mende, Space Sciences Laboratory, University of California, Centennial Drive at Grizzly Peak Blvd., Berkeley, CA 94720-7450, USA. (mende@ssl.berkeley.edu)

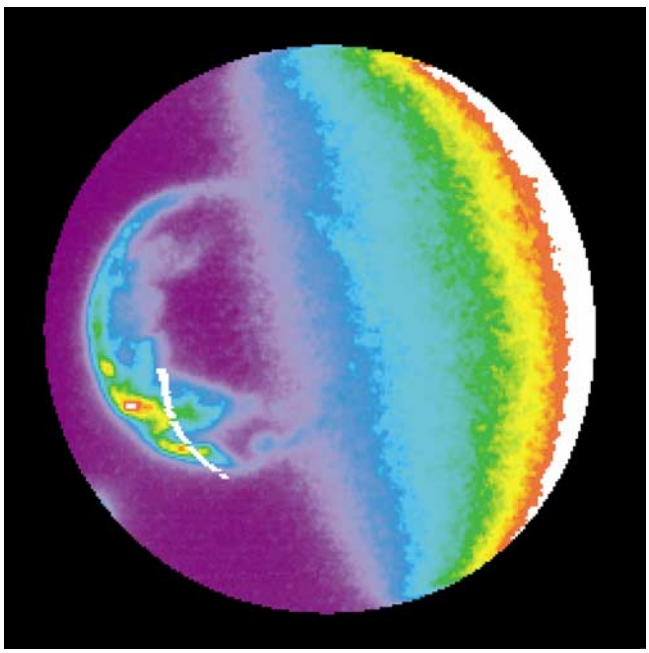

Figure 3. WIC image of the North polar region obtained on 21 October 2001 at 1727 UT. The white segment shows the track of the NOAA 16 orbit projected at 120 km. The spacecraft moved equatorward across the auroral oval.

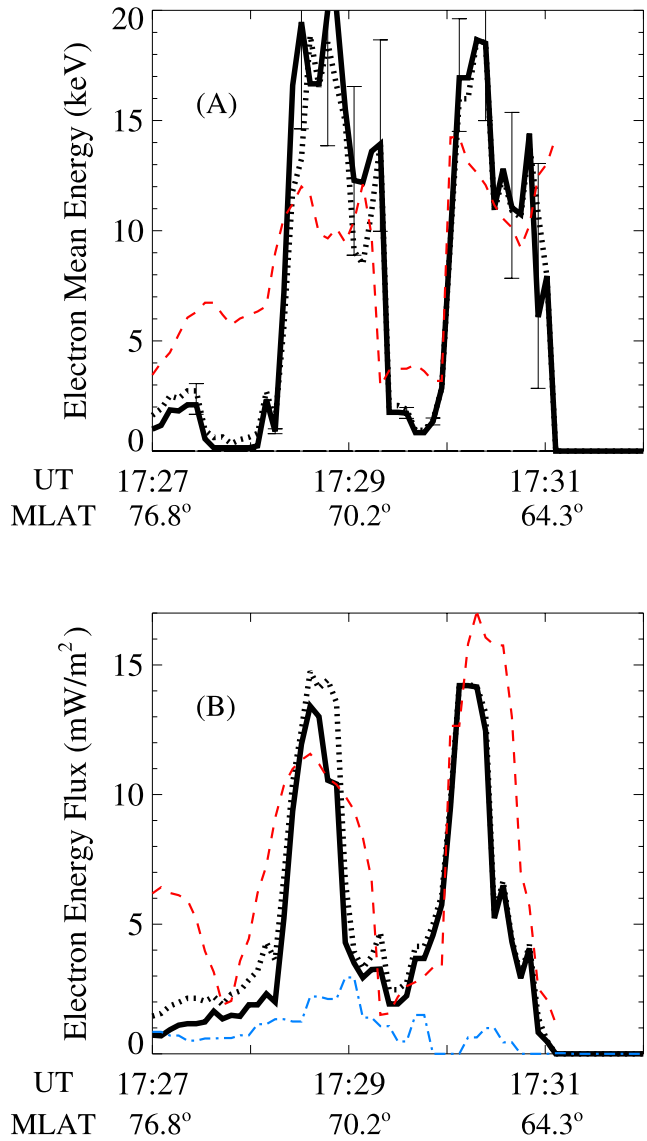

Figure 4. Distribution of the mean electron energy (a) and energy flux (b) deduced from simultaneous WIC, SI12, and SI13 images on 21 October 2001 (as shown in Figure 3). The dark thick solid line is for a 8 keV mean proton energy; the dark thick dotted line is for 2 keV. For comparison, simultaneous in situ measurements from a NOAA 16 overflight are also shown (red curves). The proton energy flux measured by the NOAA particle detector multiplied by 5 is also shown in Figure 4b (blue curve).

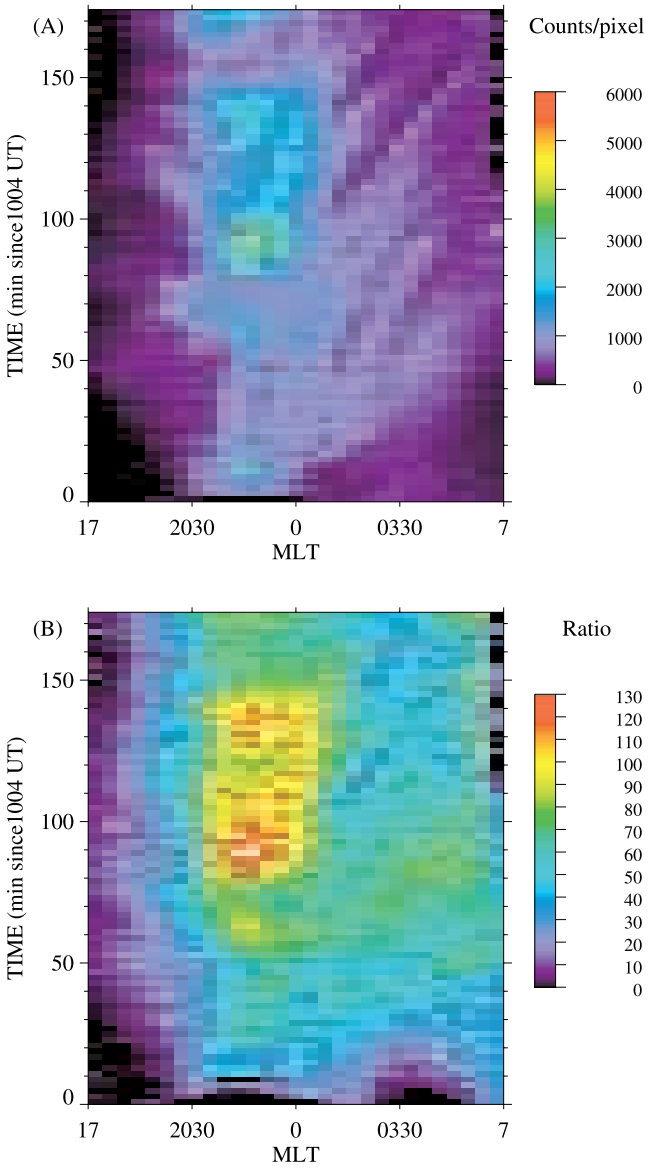

Figure 7. FUV data showing the magnetic local time distribution of two auroral substorms observed with IMAGE-FUV (on 28 October 2000 from 1004 to 1300 UT). (a) WIC counts and (b) corrected WIC/SI13 ratio. All pixels exceeding the scale upper limits are shown in white.

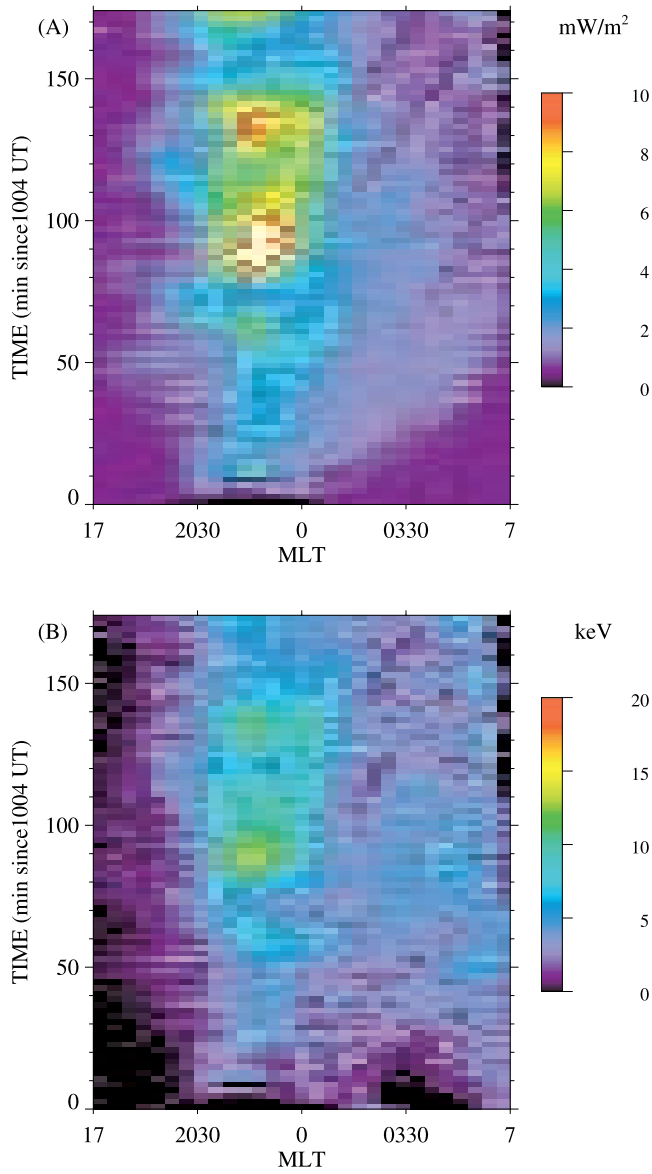

Figure 8. Characterization of the evolution of the electron precipitation during substorms deduced from FUV data. The two auroral substorms are the same as in Figure 7. (a) Precipitated electron energy flux (mW/m^2) and (b) mean electron energy (keV). Pixels with values exceeding the scale upper limits are shown in white.

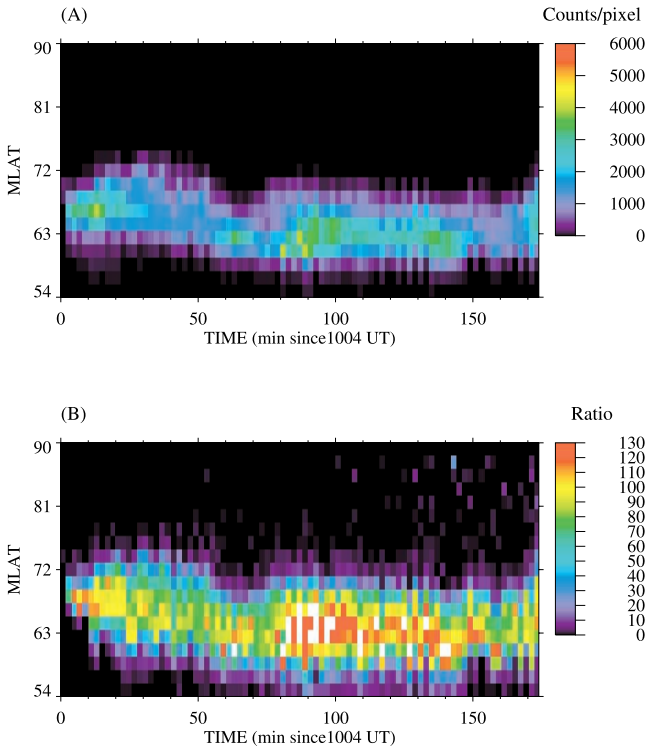

Figure 9. FUV data showing the magnetic latitudinal distribution of the two auroral substorms (28 October 2000 from 1004 to 1300 UT) in the 2100–2400 MLT sector. (a) WIC counts and (B) corrected WIC/SI13 ratio. Pixels with values exceeding the scale upper limits are shown in white.

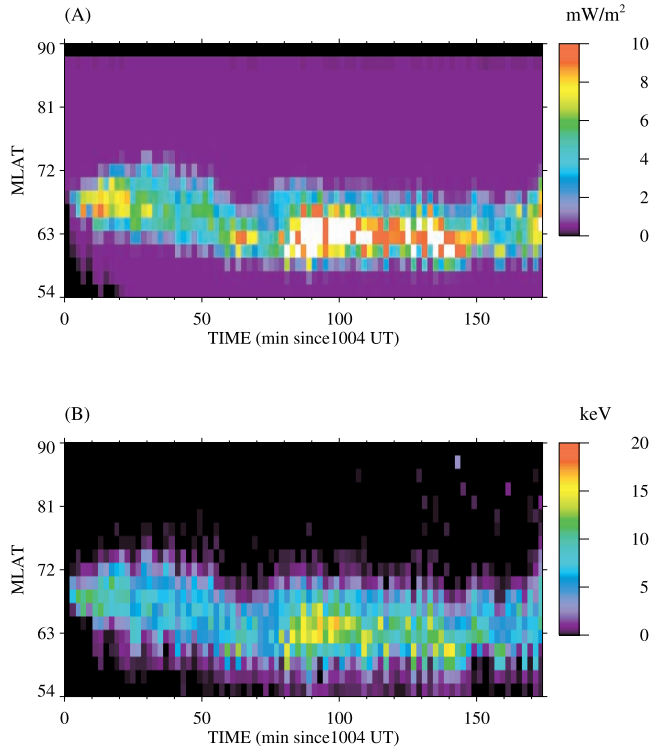

Figure 10. Characterization of the latitudinal distribution of the electron precipitation during auroral substorms deduced from FUV data. The two auroral substorms are the same as in Figure 9. The 2100–2400 MLT sector is illustrated here. (a) Electron energy flux (mW/m^2) and (b) mean electron energy (keV).

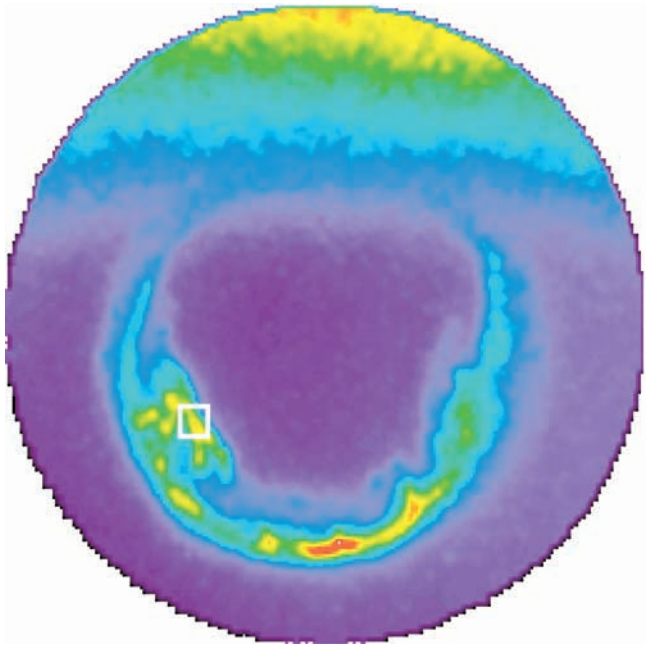

Figure 12. Location of the FAST crossing of the oval shown on the WIC image (28 October 2000) at 1120 UT.

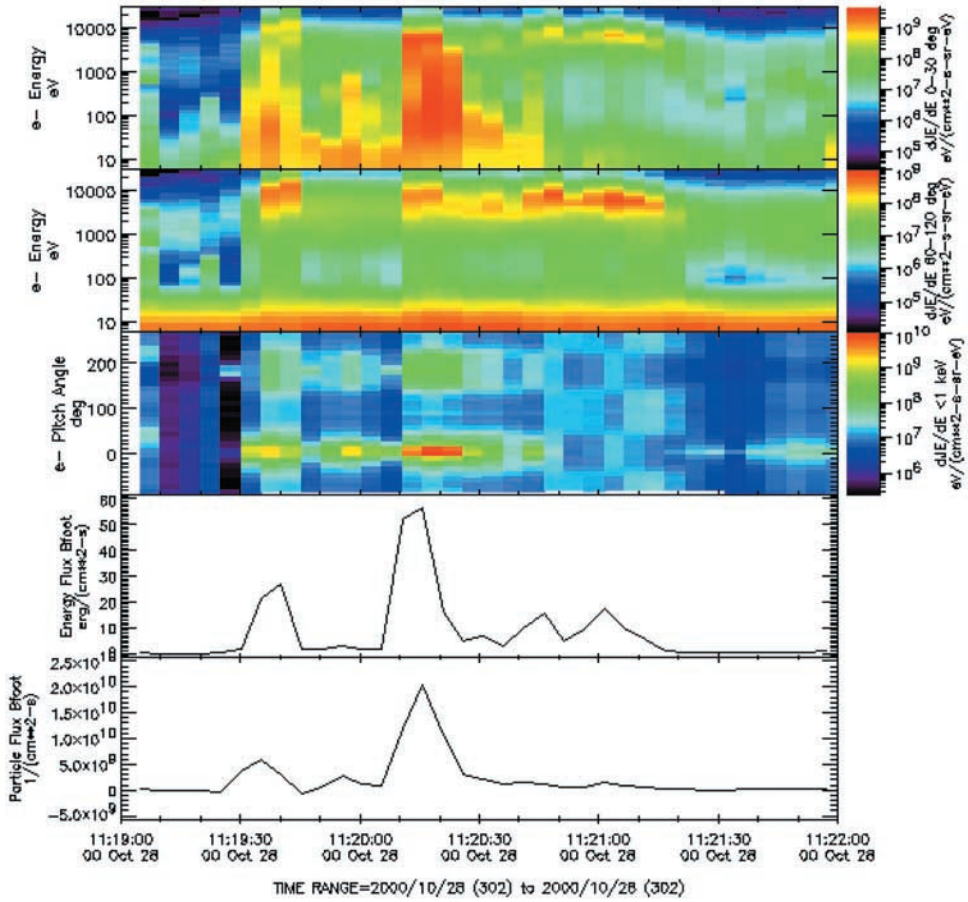

Figure 13. (top to bottom) The electron energy spectrograms, with pitch angles between 0° and 30°, 60°, and 120°, the pitch angle distribution, the energy and the number flux.

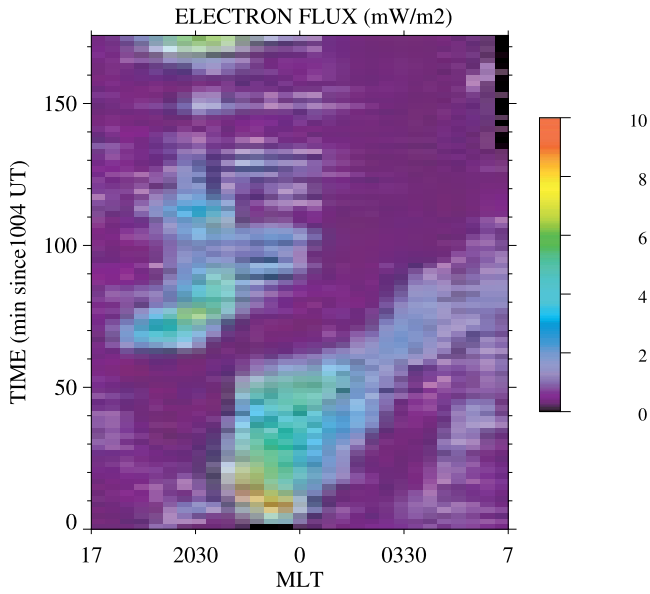

Figure 14. Electron energy flux for MLAT between 69° and 72° for the substorm of 28 October 2000 (day 302). The event observed with FAST is seen near 1900 MLT, 75 min after 1004 UT.